Forced detection Monte Carlo algorithms for accelerated blood vessel image simulations

Ingemar Fredriksson, Marcus Larsson and Tomas Strömberg

Forced Detection Monte Carlo Algorithms for Accelerated Blood Vessel Image Simulations

Ingemar Fredriksson[*]*, Marcus Larsson, and Tomas Strömberg*

Department of Biomedical Engineering, Linköping University, S-581 85 Linköping, Sweden

Keywords: Monte Carlo simulations; Diffuse scattering; Variance reduction; Image simulation

PACS: 02.70.Uu Applications of Monte Carlo methods, 11.80.La Multiple scattering, 87.55.K- Monte Carlo methods, 87.63.L- Visual imaging

Two forced detection (FD) variance reduction Monte Carlo algorithms for image simulations of tissue-embedded objects with matched refractive index are presented. The principle of the algorithms is to force a fraction of the photon weight to the detector at each and every scattering event. The fractional weight is given by the probability for the photon to reach the detector without further interactions. Two imaging setups are applied to a tissue model including blood vessels, where the FD algorithms produce identical results as traditional brute force simulations, while being accelerated with two orders of magnitude. Extending the methods to include refraction mismatches is discussed.

1. Introduction

The Monte Carlo (MC) method is a stochastic numerical technique that, based on random numbers, solves mathematical and physical problems. In biophotonics, where the diffusion approximation occasionally is inadequate to solve the transport equation accurately, light transport can be simulated by tracing a large number of individual photon random walks using the MC method. Thorough, basic descriptions of the method in biophotonics have been given previously [1,2].

To reduce the computational time needed to achieve a certain variance in a simulation, several variance reduction methods can be employed. The most common method is to assign a weight to each photon, where a part of the photon is absorbed in each step [1]. When using photon weights, a Russian roulette is applied to terminate most photons with weights below a certain threshold value [1,3]. This method can also be used when the photon reaches an uninteresting region, for example far from the detector. A related method is to split the photon when it reaches an interesting region or property [3,4]. The photon is then split into s new photons, each with $1/s$ of the weight, that follow individual paths. Other variance reduction methods involve convolution of the light emitting beam [2], and taking advantage of rotational symmetry in the model [5]. The latter methods are valid for layered simulation models only. In cases were very few photons are detected, the result can be improved drastically by using a biased artificial phase function that forces the photons towards the detector. This is sometimes refereed to as controlled MC [6] or angle biased MC [7].

Another variance reduction method, foremost used in atmospheric optics, nuclear and particle physics, and radiology, is forced detection (FD) [8-12]. This method is useful when the probability for a photon to hit the detector is very low [12]. With this method, a part of the photon is forced to reach the detector at each and every scattering event. The method has also been successfully used for optical MC simulations of homogenous media [8,12].

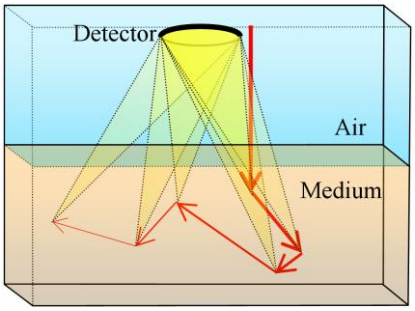

The principle of forced detection; a part of the photon weight, based on the probability of reaching the detector without further interactions, is forced to the detector at each and every scattering event.

However, its potential of accelerating image simulations [13] has not been demonstrated. Neither has it been shown that FD can accelerate simulations of more complex geometries, something that is needed in applications such as diffuse optical tomography [6]. Therefore, the aim of this article is to give detailed descriptions of two FD algorithms for simulation of optical imaging. The presented algorithms are evaluated in two imaging setups where the absorption from blood vessels embedded in tissue, with matched refractive indices, is simulated. The FD simulations generated identical results as compared to classical brute force (i.e. non-accelerated) MC simulations, with simulation times two orders of magnitude shorter. The discussion covers some precautions for using FD, and describes situations where it can be expected

to be efficient. It also addresses the fact that the algorithms do not account for general refractive index mismatches between objects.

2. Materials and methods

The MC software used is an in-house software based on [1,2], with extended functionality to handle various geometries (cylinders, boxes) and Doppler shifts. The software, which has been validated to [2], has previously been used in [4,14].

2.1 Forced detection

Two algorithms of FD, where the probability for a photon to reach the detector without any further interactions is calculated at each scattering event, are implemented and evaluated. This probability depends on: the detector geometry, the scattering phase function, the scattering and absorption coefficients, and the Fresnel reflection. Based on these probabilities, a fraction of the photon weight is forced to the detector (termed *forced photon*) while the remaining photon weight continues its random walk. The same procedure is repeated for all scattering events until the photon is terminated by either a roulette or by exiting the perimeter of the geometrical model. The first algorithm, suitable for simulations of setups containing ordinary (e.g. non-telecentric) lens systems, consists of the following steps, generally performed at each scattering event:

1. N points are selected (randomly or in some deterministic manner) on the detector surface. Each of these points represent a fractional area, $a_{\text{det}} = A_{\text{det}} / N$, of the total detector surface A_{det}. Steps 2-10 are repeated for each of these detector points.
2. The direction $\hat{\boldsymbol{\mu}}_{\text{det}}$ and distance r between the scattering point and the detector point is calculated.
3. The cosine of the deflection angle θ between the incident photon direction, $\hat{\boldsymbol{\mu}}_{\text{i}}$, and $\hat{\boldsymbol{\mu}}_{\text{det}}$ is calculated as $\cos\theta = \hat{\boldsymbol{\mu}}_{\text{i}} \cdot \hat{\boldsymbol{\mu}}_{\text{det}}$ (Fig. 1a). In analogy, the cosine of the angle ψ between the detector normal $\hat{\mathbf{n}}_{\text{det}}$ and $\hat{\boldsymbol{\mu}}_{\text{det}}$ is calculated as $\cos\psi = \hat{\mathbf{n}}_{\text{det}} \cdot \hat{\boldsymbol{\mu}}_{\text{det}}$ (Fig. 1b). If ψ is not within the acceptance angle of the detector, the probability P_{t} of reaching the detector is set to 0 and no photon weight is detected.

Fig. 1 a) Incident photon, with a direction $\hat{\boldsymbol{\mu}}_{\text{i}}$, is scattered in the center of the unit sphere. The forced part of the photon is directed towards the detector ($\hat{\boldsymbol{\mu}}_{\text{det}}$) located at a distance r. b) Cross section where the plane spanned by $\hat{\mathbf{n}}_{\text{det}}$ and $\hat{\boldsymbol{\mu}}_{\text{det}}$ intersects the unit sphere in a).

4. The probability $P_{\text{d}\Omega}$ of being scattered within the solid angle dΩ (Fig. 1a) is expressed as:

$$P_{\text{d}\Omega} = p_\theta(\cos\theta)\,\text{d}\Omega, \tag{1}$$

where $p_\theta(\cos\theta)$ is the scattering phase function that fulfills $2\pi\int_{-1}^{1} p_\theta(\cos\theta)\text{d}(\cos\theta) = 1$. Eq. (1) holds under the assumption that $p_\theta(\cos\theta)$ is constant within dΩ. Assuming that dΩ is small, the relation between dΩ and the fractional area a_{det} is (Fig. 1b):

$$\text{d}\Omega = a_{\text{det}}\cos\psi / r^2 = A_{\text{det}}\cos\psi /(r^2 N). \tag{2}$$

Thus, the probability $P_{\text{d}\Omega}$ that the forced photon is scattered towards a_{det} is expressed as:

$$P_{\text{d}\Omega} = p_\theta(\cos\theta)\,\text{d}\Omega = p_\theta(\cos\theta)A_{\text{det}}\cos\psi /(r^2 N). \tag{3}$$

5. For further acceleration, a roulette is performed for forced photons with a low $P_{\text{d}\Omega}$. If $P_{\text{d}\Omega} < \varepsilon$, the calculations continue from step 6 with $P_{\text{d}\Omega} = \varepsilon$ only if $\xi < P_{\text{d}\Omega} / \varepsilon$, where ε is the threshold of the roulette and $\xi \in [0, 1)$ is a random number, else $P_{\text{d}\Omega} = 0$. This ensures photon weight conservation.
6. The probability, P_{s}, to reach the fractional detector area a_{det} without further scattering is given by Beer-Lambert's law:

$$P_{\text{s}} = \exp(-\textstyle\sum_l^L d_l \mu_{\text{s},l}), \tag{4}$$

where L is the number of objects in the model between the scattering point and detector point, d_l is the pathlength in object l, and $\mu_{s,l}$ is the scattering coefficient in object l. In analogy, the probability of not being absorbed, P_{a}, is calculated by substituting $\mu_{\text{s},l}$ to $\mu_{\text{a},l}$ in Eq. (4), where $\mu_{\text{a},l}$ is the absorption coefficient in object l.
7. The probability P_{Fresnel}, that no reflection occurs in the borders between objects, is given by Fresnel's law. When the refractive indices are matched, $P_{\text{Fresnel}} = 1$.
8. The total probability, P_{t}, to be scattered within dΩ and to reach the detector without further scattering or reflection, is given by $P_{\text{t}} = P_{\text{d}\Omega} P_{\text{s}} P_{\text{Fresnel}}$.
9. A forced photon is detected with the weight $w_{\text{det}} = w_0 P_{\text{a}} P_{\text{t}}$, where w_0 is the current weight of the photon.
10. A roulette is performed for forced photons with a low w_{det}. This is done in analogy with step 5, with the threshold ζ. The difference between the roulette at step 5 and this roulette is that the former increases the speed of the simulations, whereas the latter foremost prevents unnecessary storage.
11. When the forced photon weights w_{det} have been detected at the N detector points, the photon continues its random walk as in normal MC, with its weight reduced

according to $w_{cont} = w_0(1 - \sum^{N} P_t)$. However, the photon is not allowed to reach the detector without further interaction. If it does, then the photon is returned to the current scattering position and a new scattering direction and step size is chosen.

The first four steps can be modified as follows, to give another variant of FD that is suitable for simulating setups where all detector points has the same acceptance cone (e.g. fibers and telecentric lens systems):

1. N directions (from the location of the scattering event) are selected within the acceptance angle α from the detector normal $\hat{\mathbf{n}}_{det}$. If a direction is not intersecting the detector surface, the probability P_t is set to 0 and no photon weight is detected. For the remaining directions, with detector intersecting points that represent a fractional detector area $a_{det} \propto 1 / N$, steps 2-10 are repeated.
2. $\hat{\boldsymbol{\mu}}_{det}$ and $\cos\theta$ are calculated according to points 2 and 3 above.
3. The acceptance angle α and N give the solid angle $d\Omega$ in Eq. (1) as the area of a spherical cap divided by N:

$$d\Omega = 2\pi(1-\cos\alpha)/N\,. \qquad (5)$$

Thus, the probability $P_{d\Omega}$ that the forced photon is scattered towards the area a_{det} can be expressed as:

$$P_{PF} = p_\theta(\cos\theta)\,d\Omega = p_\theta(\cos\theta)2\pi(1-\cos\alpha)/N\,. \qquad (6)$$

4. Continue from step 5 in the first FD algorithm.

2.2 Simulations

To evaluate the performance of the two FD algorithms, and to demonstrate their applicability, an MC model was developed. The model consisted of two blood vessels submerged in dermal tissue. The dermal tissue had its surface at $z = 0$, being infinitely thick and infinite in x and y directions. Both blood vessels were located with their center axes along the x-axis. The larger blood vessel, 200 µm inner diameter, was placed at a depth $z = 700$ µm (vessel center) and $y = 0$ mm (*LV* in Fig. 2a), and the smaller blood vessel, 40 µm inner diameter, at $z = 150$ µm and $y = 1.5$ mm (*SV* in Fig. 2a). The blood vessels contained 100 % blood, whereas the dermal tissue consisted of 0.2 % homogeneously distributed blood. The optical properties of the dermal tissue and the blood (80 % oxygen saturation, 42 % hematocrit) are valid at 543 nm, a common laser wavelength where the absorption of blood is high, and summarized in Table 1. The Henyey-Greenstein phase function was employed for modeling scattering angles in the dermal tissue, whereas the two-parametric Gegenbauer kernel phase function [15] with $g_{Gk} = 0.951$ and $\alpha_{Gk} = 1.0$ was used for the blood. The optical properties were collected as in [4], but at 543 nm. All objects in the simulation model, including the air-layer above the dermal tissue, had matched refractive indices.

Table 1 Optical properties of the simulated tissue.

	μ_a [mm^{-1}]	μ_s [mm^{-1}]	g [-][a]
Dermis	0.25	25	0.85
Blood (80 % HbO_2)	36.4	292	0.992

[a] g is the anisotropy factor, i.e. the mean cosine of the scattering angle

Two setups using this model were simulated. In both setups, the tissue was homogeneously illuminated over an 8 × 8 mm area (*IA* in Fig. 2a). In setup I, the camera setup in Fig. 2b was simulated (ordinary lens system) by placing the detector at the position of the lens. The lens in the camera setup had a focal length $f_{lens} = 40$ mm and a working distance (object conjugate) $s_1 = 200$ mm, giving a magnification of $f_{lens} / (s_1 - f_{lens}) = 0.25$, and an image conjugate $s_2 = s_1 f_{lens} / (s_1 - f_{lens}) = 50$ mm. Furthermore, the lens was stopped down to an F-number $N_{lens} = 8.0$, for an increased depth-of-field. This resulted in a detecting aperture D_{lens} (diameter) of $f_{lens} / N_{lens} = 5.0$ mm. In setup II, consisting of a similar camera setup but with a telecentric lens system, only photons within the acceptance angle $\alpha = 0.0125$ rad were detected. In both setups, this resulted in $d\Omega \approx 4.9 \times 10^{-4}$ (see equations 2 and 5 with $N = 1$). For setup II, $d\Omega$ is constant as it is given by the acceptance angle and the N random directions, whereas it varies somewhat for setup I (r and ψ varies slightly).

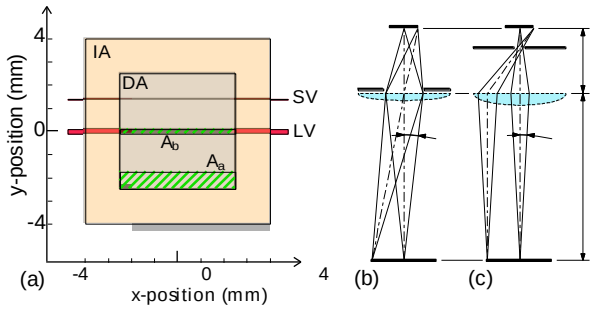

Fig. 2 The simulated tissue model (a), and lens setups I (b) and II (c). Note that the sketches in (b) and (c) are not according to scale (e.g. α in b and c is similar in the simulations). The light is injected at *IA*, an 8×8mm area; the light escaping the tissue from the area *DA* is detected at the position of the lenses; *SV* and *LV* are the small superficial and the large deeper lying vessels, respectively; the striped areas A_a and A_b are used in the CNR calculation.

The detected photons in both setups were back-traced to the object plane, in this case located on the tissue surface ($z = 0$ mm). Based on the coordinates where the back-traced photons intersected the object plane, images were formed by binning the detected light intensity into 100 × 100 pixels with a resolution of 50 µm/pixel. This resulted in images of a 5 × 5 mm area (*DA* in Fig. 2a).

The quality of a simulated image was determined by the contrast to noise ratio (*CNR*) between two areas (A_a and A_b in Fig. 2a). This ratio was calculated as $CNR = (s_a - s_b) / \sigma_a$, where s_a is the mean intensity in area

A_a, s_b is the mean intensity in area A_b and σ_a is the standard deviation in area A_a. The simulation times for achieving a *CNR* = 2.0 was used as a performance measure when comparing the FD algorithms (variant I in setup I and variant II in setup II) with classical brute force MC simulations. All simulations were performed on an Intel® Core™2 Duo processor at 2.13 GHz.

A traditional roulette, affecting photons when their weight dropped below 0.1 with a 0.1 chance of surviving, was used in all simulations. The roulette limit ζ at step 10 was chosen so that $\sum w_{det}|_{w_{det}<\zeta} = \sum w_{det}|_{w_{det}>\zeta}$, where w_{det} is the detected photon weight (see also Eq. 9). The limit, ε, for the roulette at step 5 was chosen as $\varepsilon = 5\zeta$. The value of ζ was decided from a small set of trial simulations for each setup, giving $\zeta_I = 4.0 \times 10^{-4}$ and $\zeta_{II} = 1.2 \times 10^{-4}$ for setups I and II, respectively. These limits were empirically chosen to achieve short simulation times. The number of random points/directions at step 1 in the algorithms was chosen to $N = 1$.

A third setup was also created to test the sensitivity of the detected intensity to the magnitude of $d\Omega$. This setup consisted of a 1.0 mm thick slab with $\mu_a = 1.0$ mm^{-1}, $\mu_s = 10$ mm^{-1}, matched refractive index, and a Henyey-Greenstein scattering phase function with an anisotropy factor at 0.0, 0.7, and 0.9. The photons were injected perpendicular to the surface of the medium, and all photons backscattered to the surface within a certain solid angle Ω_{det} were detected (i.e. algorithm II). The solid angle was set to 0.0001×5^n, $n = 0, 1, \ldots, 6$ ($n = 6 \rightarrow \Omega_{det} \approx \pi / 2$). The various configurations of setup III were simulated with brute force (1×10^6 photons detected) and FD algorithm II (1×10^8 photons detected). In the FD simulations, $\varepsilon = 1 \times 10^{-8}$ and $\zeta = 1 \times 10^{-10}$ was used for the internal roulettes. For $g = 0.0$ and $g = 0.7$, N was set to 1, whereas for $g = 0.9$, N was set to 1, 5, or 25.

3. Results

To achieve a CNR of 2.0 between area A_a and A_b in setup I, 9.9×10^7 photons had to be emitted (4.1×10^6 detected) with the FD algorithm I, taking 9.5 hours. With the brute force technique, 6.0×10^{10} photons had to be emitted (2.7×10^6 detected), taking 573 hours. Thus, the FD algorithm accelerated the simulations with a factor of about 60, for that particular setup.

To achieve the same CNR in setup II, 5.9×10^7 photons had to be emitted (6.5×10^6 detected) with the FD algorithm II, taking 5.7 hours. With the brute force technique, 7.1×10^{10} photons had to be emitted (3.2×10^6 detected), taking 682 hours. Hence, the FD algorithm was about 120 times faster than brute force for that particular setup.

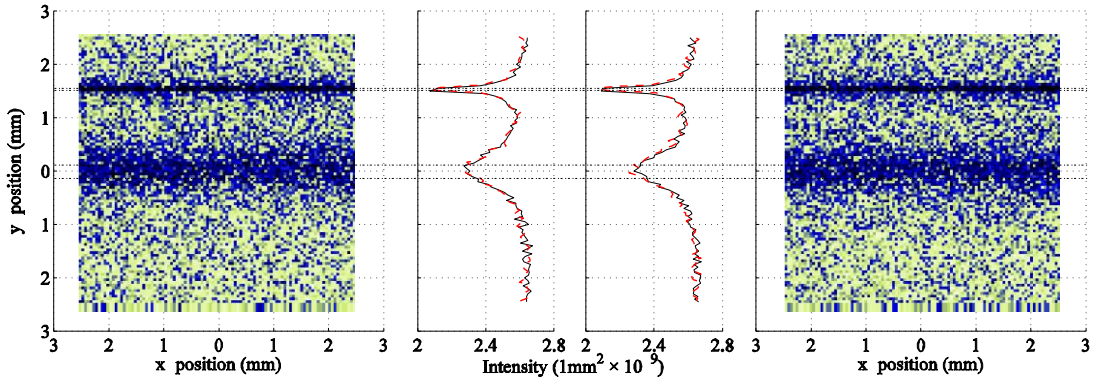

Fig. 3 The generated images from the FD algorithm of setup I (left) and of setup II (right), and the average intensity over the x-direction for both brute force (solid black) and forced detection (dashed red) simulations (left middle - setup I; right middle - setup II). The borders of the blood vessels are marked with the dash-dotted lines.

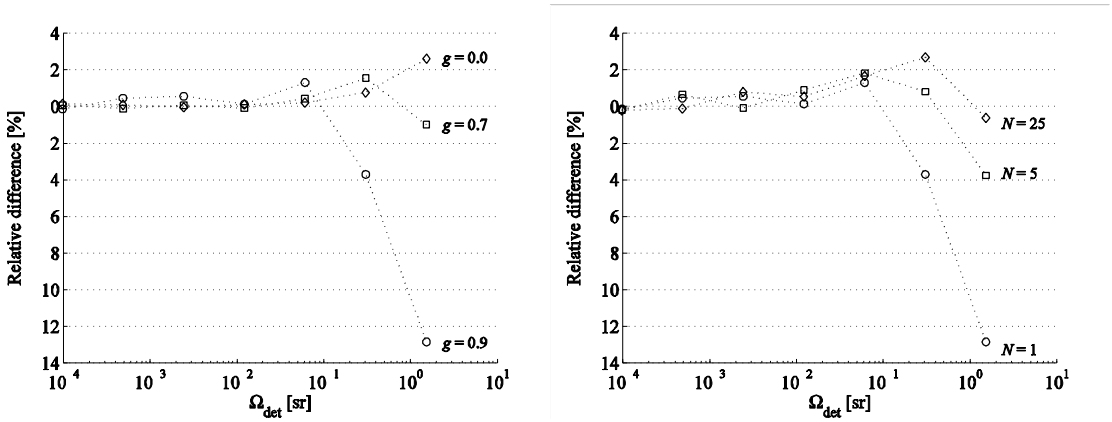

Fig. 4 Relative differences in detected intensity between FD and brute force simulations of setup III as a function of acceptance solid angle Ω_{det}. Three different values of g with $N = 1$ are shown in the left panel, and three different values of N with $g = 0.9$ are shown in the right panel.

Two examples of simulated images are shown in Fig. 3. The FD algorithms and the brute force simulations gave identical results, except for the stochastic noise (Fig. 3 middle). The two lens setups generated essentially the same results.

Fig. 4 shows the relative difference in the detected backscattered intensity between brute force and FD simulations of setup III, for various acceptance solid angles Ω_{det} ($d\Omega = \Omega_{det} / N$, Eq. 5).

4. Discussion

It is assumed that $p_\theta(\cos\theta)$ is constant or representative within the solid angle $d\Omega$, defined by Eq. (2) and Eq. (5), in both algorithms, and similar assumptions are made for P_s, P_a, and $P_{Fresnel}$. These assumptions are valid if $d\Omega$ is sufficiently small. If this is not true, the probability P_t of reaching the specific detector point is an inadequate representation of the probability of reaching the fractional detector area a_{det}, which will lead to erroneous simulation results. A natural strategy to ensure that $d\Omega$ is sufficiently small is to increase the number of random points N. However, increasing N also increases the simulation time, jeopardizing the efficiency of the FD algorithms. Similar strategies have previously been outlined by others [8,12], but they do not report which $d\Omega$ level that is needed to produce accurate simulation results.

Fig. 4 shows that the accuracy of the FD algorithm deteriorates for $d\Omega > 0.1$ ($d\Omega = \Omega_{det} / N$). In the case where $g = 0.0$, this is due to a non-constant P_s and P_a within $d\Omega$. This results in an overestimated total detected intensity for high $d\Omega$. For $g = 0.7$ and especially $g = 0.9$, $p_\theta(\cos\theta)$ is not constant within $d\Omega$, which, in our setup, results in an underestimated total detected intensity for large $d\Omega$. The results also show that the simulation outcome is more accurate when decreasing $d\Omega$ by increasing N. When $N > 1$ is required for a sufficiently small $d\Omega$, for example when the photon is scattered near the detector in algorithm I, N can be chosen adaptively to ensure that $d\Omega$ in Eq. (2) is sufficiently small, without N being unnecessarily large.

The arguments above imply that the FD algorithms are accurate when $d\Omega$ is small and the acceleration is effective when N is small. For algorithm I, this is true when the distance from all scattering events to the detector is large in comparison to the area of the detector surface (Eq. 2). For algorithm II, this is true when the acceptance angle is small (Eq. 5). It is therefore expected that the methods are efficient and accurate for the two simulated setups presented in this article, where $d\Omega \approx 4.9 \times 10^{-4}$. Algorithm I in particular can also be expected to be highly efficient for setups with a small detector placed far away from the scattering medium, which is for example the situation in a laser Doppler perfusion imager. The presented FD methods are, however, not expected to be efficient or accurate for setups where a fiber probe is used in contact measurements, since a scattering position can be very close to the fiber tip, giving rise to a large $d\Omega$ in algorithm I, and the acceptance angle is often too large to give a sufficiently small $d\Omega$ in algorithm II.

Some remarks are necessary for the selection of the N points or directions at step 1 in the algorithms. It may be appealing to choose a large N to simultaneously contribute to several detector pixels. However, in setups I and II, all directions from a given scattering position to any point on the detector (the lens) will cross the object plane (the tissue surface) in essentially the same position, and thus contribute to the same pixel in the simulated image. To avoid any biasing in the simulations, it is natural to choose the N points or directions randomly when $N = 1$. However, they do not need to be randomly chosen at each scattering event, but may be chosen before emitting every M:th photon for any appropriate M. The latter modification was used in the presented example simulations, with $M = 2000$. For other situations though, when

it makes sense to choose a larger N, it could be wise to select the points or directions as uniform as possible.

The FD algorithms described do not fully handle refractive index mismatches. Therefore, all media in the two example setups had a matched refractive index. We have seen that ignoring refractive index mismatches may lead to erroneous results, even when the mismatch is small. The divergence is especially pronounced when reflecting objects are placed superficially in the medium. In some situations, the algorithms can be modified to handle mismatches. When the only mismatch is between the simulated medium and air, an approximate solution could be used where the position of the detector, in respect to the medium/air boundary, is adjusted with a factor $f = n_{\text{medium}} / n_{\text{air}}$. The acceptance angle should also be adjusted. One can then expect to achieve accurate simulation results for incidence angles < 0.1 rad for $f < 1.5$. The idea of a more general solution that works in layered setups has been presented before [12]. By using Snell's and Fresnell's laws, this can be generalized to work with any arbitrary geometry, but it will most likely be computationally inefficient for complex geometries. On the other hand, within the field of biophotonics, borders between objects are often rough or wavy. Hence, simulating smooth, plane borders with Snell refraction could possibly introduce erroneous results, worse than the errors introduced by ignoring refractive index mismatches. This is supported by the findings by Meglinski and Matcher [16]. They concluded that when the borders between layers with refractive index mismatch are wavy, photons go deeper into the medium. The same effect is expected when ignoring the refractive index mismatch.

5. Conclusions

Two different FD algorithms have been presented in detail. The algorithms were tested for two different imaging setups of tissue-embedded objects with matched refractive index, and compared to classical brute force MC simulations. The resulting images were identical except for the stochastic noise, showing that FD can be used for accurate image simulations of blood vessels embedded in tissue as long as $d\Omega < 0.1$. The efficiency of FD acceleration is demonstrated by the reduced simulation time with two orders of magnitude to achieve the same contrast to noise ratio in the images.

Acknowledgements

The project was supported by the NIMED Center for Biomedical Data Processing, where this project was funded by Linköping University and Perimed AB.

Ingemar Fredriksson received his M.Sc. in 2004, and is currently a Ph.D. student at the Department of Biomedical Engineering, Linköping University, Sweden. His research covers modeling and simulation of light transport in tissue, with applications in laser Doppler flowmetry and diffuse reflectance spectroscopy.

Marcus Larsson received his M.Sc. in 1999 and his Ph.D. in 2006. He is currently holding a post doctor position at the Department of Biomedical Engineering, Linköping University, Sweden. His main research interests are within theoretical and applied biomedical optics, currently including laser Doppler flowmetry, diffuse reflectance spectroscopy and photon transport simulations.

Tomas Strömberg graduated in 1989, received his PhD in 1996, and became professor of Biomedical Engineering in 2003 at Linköping University in Sweden. His main fields of research are modeling and applications of biomedical optics within laser Doppler flowmetry and diffuse reflectance spectroscopy.

References

[1] Prahl, S. A., M. Keijzer, et al. (1989). A Monte Carlo Model of Light Propagation in Tissue. SPIE Proceedings of Docimetry of Laser Radiation in Medicine and Biology.

[2] Wang, L. H., S. L. Jacques, et al. (1995). "Mcml - Monte-Carlo Modeling of Light Transport in Multilayered Tissues." Computer Methods and Programs in Biomedicine 47(2): 131-146.

[3] Veach, E. (1997). Robust Monte Carlo Methods for Light Transport Simulation. Department of Computer Science. Stanford, Stanford University.

[4] Fredriksson, I., M. Larsson, et al. (2008). "Optical microcirculatory skin model: assessed by Monte Carlo simulations paired with in vivo laser Doppler flowmetry." Journal of Biomedical Optics 13(1): 014015.

[5] Nilsson, H., M. Larsson, et al. (2002). "Photon pathlength determination based on spatially resolved diffuse reflectance." J. Biomed. Opt. 7(3): 478-485.

[6] Chen, N. G. (2007). "Controlled Monte Carlo method for light propagation in tissue of semi-infinite geometry." Applied Optics 46(10): 1597-1603.

[7] Yao, G. and L. H. V. Wang (1999). "Monte Carlo simulation of an optical coherence tomography signal in homogeneous turbid media." Physics in Medicine and Biology 44(9): 2307-2320.

[8] Meier, R. R., J.-S. Lee, et al. (1978). "Atmospheric scattering of middle UV radiation from an internal source." Applied Optics 17(20): 3216.

[9] Beck, J. W., R. J. Jaszczak, et al. (1982). "Analysis of SPECT including Scatter and Attenuation Using Sophisticated Monte Carlo Modeling Methods." IEEE Transactions on Nuclear Science 29(1): 506-511.

[10] Berrocal, E., D. Y. Churmakov, et al. (2005). "Crossed source-detector geometry for a novel spray diagnostic: Monte Carlo simulation and analytical results." Applied Optics 44(13): 2519-2529.

[11] Churmakov, D. Y., V. L. Kuzmin, et al. (2006). "Application of the vector Monte-Carlo method in polarisation optical coherence tomography." Quantum Electronics 36(11): 1009-1015.

[12] Tinet, E., S. Avrillier, et al. (1996). "Fast semianalytical Monte Carlo simulation for time-resolved light propagation in turbid media." Journal of the Optical Society of America a-Optics Image Science and Vision 13(9): 1903-1915.

[13] Chen, C., J. Q. Lu, et al. (2007). "Numerical study of reflectance imaging using a parallel Monte Carlo method." Medical Physics 34(7): 2939-2948.

[14] Fredriksson, I., M. Larsson, et al. (2006). Absolute flow velocity components in laser Doppler flowmetry. Optical Diagnostics and Sensing VI, San Jose, CA, USA, SPIE.

[15] Reynolds, L. O. and N. J. McCormick (1980). "Approximate two-parameter phase function for light scattering." Journal of the Optical Society of America 70(10): 1206-1212.

[16] Meglinsky, I. V. and S. J. Matcher (2001). "Modelling the sampling volume for skin blood oxygenation measurements." Medical & Biological Engineering & Computing 39(1): 44-50.